

## Subsalt imaging for exploration, production, and development: A review

Jacques P. Leveille<sup>1</sup>, Ian F. Jones<sup>2</sup>, Zheng-Zheng Zhou<sup>2</sup>, Bin Wang<sup>3</sup>, and Faqi Liu<sup>4</sup>

### ABSTRACT

The field of subsalt imaging has evolved rapidly in the last decade, thanks in part to the availability of low cost massive computing infrastructure, and also to the development of new seismic acquisition techniques that try to mitigate the problems caused by the presence of salt. This paper serves as an introduction to the special Geophysics section on *Subsalt Imaging for E&P*. The purpose of the special section is to bring together practitioners of subsalt imaging in the wider sense, i.e., not only algorithm developers, but also the interpretation community that utilizes the latest technology to carry out subsalt exploration and development. The purpose of the paper is in many ways pedagogical and historical. We address the question of what subsalt imaging is and discuss the physics of the subsalt imaging problem, especially the illumination issue. After a discussion of the problem, we then give a review of the main algorithms that have been developed and implemented within the last decade, namely Kirchhoff and Beam imaging, one-way wavefield extrapolation

methods and the full two-way reverse time migration. This review is not meant to be exhaustive, and is qualitative to make it accessible to a wide audience. For each method and algorithm we highlight the benefits and the weaknesses. We then address the imaging conditions that are a fundamental part of each imaging algorithm. While we dive into more technical detail, the section should still be accessible to a wide audience. Gathers of various sorts are introduced and their usage explained. Model building and velocity update strategies and tools are presented next. Finally, the last section shows a few results from specific algorithms. The latest techniques such as waveform inversion or the “dirty salt” techniques will not be covered, as they will be elaborated upon by other authors in the special section. With the massive effort that the industry has devoted to this field, much remains to be done to give interpreters the accurate detailed images of the subsurface that are needed. In that sense the salt is still winning, although the next decade will most likely change this situation.

### INTRODUCTION

Energy companies are constantly pushing into different and usually more challenging environments in the search for hydrocarbons worldwide. For quite a while now, salt basins worldwide have been one of the places to find the most prospective hydrocarbon reserves. The best-known salt basins are probably in the Gulf of Mexico, where recent activity has led to a large number of discoveries, and the salt basins of the West African Margin, such as Angola and Gabon, which have been well explored and prolific. Recently, the subsalt basins of the Brazilian margins have seen gigantic discoveries such as Tupi, where billions of barrels of oil in place have been discovered.

Salt basins, especially tertiary basins with mobilized salt, are notoriously difficult places to explore because of the traditionally poor subsurface images typically obtained around and below salt. In this paper, we review the geophysical reasons for these difficulties in imaging and the steady progress that has been made. These reasons will, in general, be different depending on the details of the salt and on the geological history of the basins, but reasonable generalizations can be made.

The difficulties encountered by everyone in the industry in the past prompted various groups to start working together to try and solve these difficult imaging problems. In 2005, a special two day workshop was organized at the Colorado School of Mines, with a very different purpose: The organizers asked everyone to bring only

Manuscript received by the Editor 1 May 2011; revised manuscript received 3 June 2011; published online 22 November 2011.

<sup>1</sup>ION Geophysical, Houston, Texas, USA, E-mail: jacques.levaille@iongeo.com.

<sup>2</sup>ION/ GX Technology, Houston, Texas, USA, E-mail: ian.jones@iongeo.com; Zheng.Zhou@iongeo.com.

<sup>3</sup>TGS NOPEC, Houston, Texas, USA., E-mail: Bin.Wang@tgsnopec.com.

<sup>4</sup>Hess Corporation, Houston, Texas, USA, E-mail: fliu@hess.com.

© 2011 Society of Exploration Geophysicists. All rights reserved.

problems related to subsalt imaging, not solutions. The idea was to lay all the problems on the table, with the hope that exposing these problems would spur on ideas, especially in academic circles, and accelerate the pace of research in this subject. In the 17 talks presented in that workshop, gloom was apparent in every corner, with difficulties encountered above salt, near salt, and subsalt. The base of salt was disappearing without good explanations, and the subsalt images were less than clear. (Leveille et al., 2005). This led Paul Singer of then Total to ask his often repeated question: "Is the salt winning?" Although the answer in 2005 was probably yes, a fantastic amount of new techniques have been developed since that time, and it looks very much as if the E&P industry is on the verge of winning, although much more progress will be needed to fully help in the drilling of subsalt prospects which remain to this day a costly and risky enterprise. While most of the progress originally came through new seismic acquisition techniques, such as wide-azimuth surveys, rich-azimuth surveys, and a resulting alphabet soup of specialized wide azimuth acquisitions, imaging through the incorporation of better physics came in the form of reverse time migration (RTM) with full anisotropy. In this review, we will not review in any detail the recently developed acquisition techniques themselves, but rather refer the reader to the existing literature (see e.g. Corcoran et al., 2007; Howard and Moldoveanu 2006; Moldoveanu et al., 2008). Instead, we will highlight the problems that necessitated these new techniques and what the new results based on these techniques look like.

In this review, we attempt to summarize the wide-ranging field of subsalt imaging, and the progress that has been made since the early days. These will take the form of new seismic acquisition techniques and of imaging and computing techniques. The whole sub-field of subsalt velocity updating has exploded and has benefitted from these computing advances. The progress in the technology has been chronicled in a succession of successful workshops held around the globe by the SEG and the EAGE.

The computational revolution that has been going on over the last decade has allowed for the new imaging techniques to blossom, and much more is expected in the next decade. It seems that we are only limited by our imagination rather than compute cycles. However, not every subsalt problem has been solved, and many challenges remain. We will spend a little time discussing these remaining issues.

## THE PHYSICS OF SUBSALT IMAGING

Subsalt Imaging is actually a misnomer, which has been derived from the problems encountered in trying to image around and below allochthonous salt sheets in the Gulf of Mexico. The problem is trying to image below a fast velocity medium, such as salt, encased in an acoustically slow material such as tertiary sediments in the Gulf of Mexico. Similar issues will be encountered imaging through and around basalt encased in softer sediments. Before we get into the details of the difficulty encountered, it might be useful to review a few basic properties of salt tectonics.

Salt is a ubiquitous rock in many basins worldwide. Salt originally deposited in ancient times, such as the Jurassic Period in the Gulf of Mexico, and still in its original emplacement is called autochthonous. Usually, the acoustic impedance contrast between autochthonous salt and its encasing rocks is not very great, usually around 10% or less. In such cases, imaging through the autochthonous salt causes no serious problems and can be handled with a variety of

simple imaging algorithms, such as Kirchhoff techniques. That is the case for the Lou-Ann Jurassic salt in the Gulf of Mexico, still encased in Jurassic and older Cretaceous rocks. A similar situation is encountered in the North Sea with in-place Zechstein salt. In fact, that is mostly the situation as well for the recent discoveries in Brazil.

Salt is mechanically a very weak rock, and when stress is applied to it, salt can flow if given an appropriate weak conduit. It is often said that salt behaves just like toothpaste in that it flows when squeezed, but only if some opening/conduit exists, and like toothpaste it is mechanically unable to support large shear stresses. Therefore, salt does not "punch" through sediments, but rather flows along preexisting weak points if available. When salt "flows" it usually rises toward the surface, overriding sediments, and ends up forming large canopies of salt with much younger sediments surrounding it. These displaced salt bodies, not in their original emplacement of deposition, are called allochthonous and are the salt sheets that are often seen in younger tertiary basins such as the Gulf of Mexico, the West Africa basins, and many more.

The allochthonous canopies are usually formed by various episodes of salt movement. These episodes can result in very thick salt sheets, with thicknesses from a few hundred to three to five thousand meters or so. When the salt moves, it can entrain sediments with it. These sediments can be overridden by more salt, and eventually get trapped within the salt sheet. Salt sheets that "flow" can also collide and amalgamate into what looks like a larger salt sheet. Usually, sediments are trapped between the colliding salt sheets, forming what are called sutures. It is not unusual to have several sutures within what looks like a large continuous salt body.

The net result is that allochthonous salt sheets can vary in composition, from more or less pure salt, to what is now referred to as "dirty" salt containing trapped sediments called inclusions. These inclusions can vary in size from a few meters to tens of meters. Incidentally, these dirty salt inclusions are well known to salt mine engineers who detect them routinely near the edges of salt mines. These trapped sediments are usually shale material, which has been caught up as the salt moves near the surface. The trapped sediments are usually undrained sediments, and when they are encased, the water has no place to drain. As more salt or sediments are deposited over the salt, these "inclusions" become more pressurized. These inclusions can be overpressured, therefore having very low velocities, and can cause serious drilling hazards.

The composition of the material trapped in the sutures can vary widely. If the sediments are much younger, they will usually have the same properties as the inclusions discussed above. However, the sediments can also be age equivalent to the original salt, and therefore be much older, more compacted rocks. This makes sutures rather difficult to quantify a priori from a seismic velocity point of view and is still a very difficult problem.

What do we expect at the top of salt? Geologically, the salt is overriding sediments and this usually occurs near the sea floor. As such, the sediments deposited over the salt will tend to be younger than the salt. The age difference depends on the details of the timing of the salt movement. For the problem at hand, we will assume that the sediments are much younger, either Pliocene or Pleistocene. Therefore, the sediments overlying the salt will be acoustically much less compacted, and there will be a great variation in the acoustic velocities between the salt and the sediments. We will cover this in more detail below. Another thing that is

expected, is that the top of the salt will not be uniform. In fact, we should expect the top salt surface to be very rugose. This top salt rugosity is well known and follows from basic salt tectonics principles (see for example Hudec and Jackson, 2007).

In other instances, possibly large blocks of sediments can ride on top of the moving salt. These are called “rafts” or “rafted sequences,” although the newest term used to describe these sediments is “carapaces.” These carapaces can consist of varying lithologies, although the most common are shales and carbonates. Because these rafts are older sediments, their seismic velocities can be quite high, and they can be quite dense. These carapaces are not very thick, although their thickness can reach several hundreds of meters. We will not discuss these rafts any further in this review, but the practitioner of subsalt imaging must always be vigilant and consult a friendly structural geologist as to the possibility of rafts in a specific situation.

The expectation for the base salt is different. Since the salt is “overriding” existing sediments, starting from some feeder point connected to the deep “mother salt,” we expect that the base of salt surface will be reasonably smooth and flat, as deposited sediments are. Although there is variability in the base salt surface, it is indeed much smoother than the top. In fact, rapid variations in the base salt shape are more than likely associated with either the “feeder” connection to the salt sheet, with the suturing of two or more salt bodies, or with later faulting. Geologists will look closely at the discontinuity of the base of salt to detect and unravel these features. Indeed, somewhere under the salt, either near the edges toward the salt wall or anywhere under the canopy will be at least one salt feeder system. These feeders provide very useful information to the geologists trying to reconstruct the history of the basin. Unfortunately, the feeders are still difficult to image and they are usually very steeply dipping. Finally, what do we expect subsalt in terms of sediments? The answer is just about anything. The subsalt sediments will be age equivalent to the salt movement, so the age of the sediment abutting the base salt will depend on the time at which salt started to move. This leads to an interesting and complex geological problem: Depending on how many salt sheets formed the salt mass, there could be rapid variability in the age of the sediments subsalt. One salt sheet overriding Miocene sediments could easily collide with a salt sheet overriding Cretaceous sediments, with a net result of a deep Miocene subsalt basin separated from a deep cretaceous basin subsalt by some salt feeder that may or may not contain remnants of salt. This basin juxtaposition can form very good traps for hydrocarbons.

There is no limit to the number of salt sheets in principle. Although in practice, it is very rare to find more than one or two allochthonous salt sheets. Imaging through a single salt sheet is already very complex and the problem becomes increasingly more difficult with additional salt.

So the physical picture that one should carry for the remainder of this review, is that of a reasonably thick salt sheet (of order of 1–5 km), with a rugose top (with possibly rapid variations), and a reasonably flat base with several possibly sharp discontinuities. The sediments at the top of the salt sheet are usually much younger than the salt, while the subsalt sediments can really be of any age. The flank of the salt sheet will usually be very steep, although great variability can occur. This sets up the geophysical problem.

Pure salt geophysical properties are as follows: compressional velocity of 4500 m/s, a  $V_P/V_S$  ratio of 1.9 and a density of 2.16 grams/cm<sup>3</sup>. In this review, we will not focus on elastic issues,

so we will more or less ignore the shear velocity. Almost all current imaging algorithms are acoustic in nature, and most of these algorithms assume a constant density. Salt is extremely light, but very fast acoustically. For comparison, a shale with the same compressional velocity as salt would have a density of approximately 2.65 grams/cm<sup>3</sup>. The low density of the salt gives rise to a large difference in gravity signatures for salt masses. Salt also has some rather interesting electric and magnetic properties. Unfortunately, gravity and electric and magnetic phenomena will not be covered in this review.

Interestingly, basalt is also acoustically very fast, but also very dense. Compressional velocity of basalt has a wide range depending on the depositional process of the lava, but ranges from 4000 to 5000 m/s, with a density range from 2.2 to 3.0 gr/cm<sup>3</sup>. Basalt does not flow postdepositionally like salt, but obviously flows over sediments when deposited as lava. Lava flows are episodic as well, so basalt layers will be composed of thick basalt/sediment sequences. The sediments alternating with the basalt can be quite slow acoustically. This makes the basalt problem very different from the salt problem we are discussing here, although some similarity exists.

Near the top of the salt we are expecting younger sediments, with compressional velocities around 2000 m/s near the sea floor and possibly up to 3000 m/s near the top of the salt. Near the base of the salt, the range will usually be from 3000 m/s to as high as 4000–4500 m/s depending on the age of the sediments as we discussed above. It is possible (and common) to have highly overpressured sediments near the base of salt, which can have velocities even lower than 3000 m/s. Using a typical velocity-density relationship for tertiary basins we can easily convince oneself that the sediment/top salt acoustic reflection and transmission coefficients are in the range of  $R_T = 0.2–0.3$  and  $T_T = 0.7–0.9$ , respectively. A large fraction of the energy is reflected back at the top salt interface. Near the base of the salt, the reflection coefficients will be highly variable, but they will be in the range of  $R_B = 0–0.3$  and  $T_B = 0.7–1.0$ . Using the fact that a subsalt event will have a round trip down through the top of the salt and a round trip through the base of the salt, the reduction  $R_{TOTAL}$  in measured displacement which can be attributed to transmission and reflection losses only is  $R_{TOTAL} = (1 - R_B^2) * (1 - R_T^2)$ . Even with the largest reflection coefficient of 0.3, this means that the salt reflection/transmission losses will only amount to 80% or so of the incident displacement. It is often stated that the salt acts as a “partial mirror,” which is commonly misinterpreted to mean that the salt causes the energy losses simply by reflection/transmission losses, but this simple calculation shows that this is not the case. This is also why imaging through flat-layered salt is not a hard problem, which in fact could be solved using only time imaging, or poststack techniques. So, where does the difficulty in subsalt imaging come from?

Before answering that question, let us review briefly what we can expect in the case of subbasalt imaging. As we discussed earlier, basalt is not only acoustically fast, it is also very dense. If we assume that the sediments on top of the basalt are approximately 3000 m/s, and that the basalt has the same velocity as the salt (4500 m/s) but a density of 2.65 gr/cm<sup>3</sup>, then the reflection coefficient at the top of the basalt is  $R_T = 0.27$ , and the transmission  $T_T = 1 - R_T = 0.73$ , so a round trip through each interface is an attenuation of  $(1 - R_T^2) = 0.93$ . However, as we discussed, the basalt complex will be made up of many episodes of depositions, with many basalt/sediment interfaces. Assuming 10 such interfaces,

the total attenuation would be 0.5, assuming 20, it becomes 0.25. So, in some sense, purely from transmission/reflection losses, the basalt problem is much worse than the salt problem. Another effect that we do not discuss here is that the filtering effect of the basalt is to filter out most high-frequency reflections from the data. Basalt is also usually highly fractured, which compounds the losses and buries signal in scattered noise.

More importantly, the refraction angles are greatly increased or decreased because of Snell's law and the large velocity contrast. In fact, when the salt top interface is near the sea floor, the critical angle ranges from 20° to 30°. So, a beam of seismic energy coming from a shot is rapidly defocused as it passes through the salt and travels toward the salt base. Although intuitively obvious, it is hard to quantify this effect in a meaningful way, as it depends on the details of the geometry. The net result is that a fraction of the incident energy will arrive at a subsalt reflector. To compound the problem, the subsalt reflectors are in general very weak reflectors, with reflection coefficients in the 5% range, at least for a large fraction of the subsalt projects in the Gulf of Mexico. The subsalt energy that is reflected will be subject to another critical effect barrier, which can sometimes conspire to make certain reflector geometries impossible to image from certain directions, such as a reflector dipping at the critical angle relative to the salt base. Hence, the subsalt problem is two fold: necessarily weak illumination because of defocusing by the sediment-salt interface, and weak reflectivity. Signal/noise ratio (S/N) of true reflections versus scattered noise subsalt becomes critical to produce a good image in the best of cases, which requires very accurate imaging algorithms.

The illumination issues discussed above are present even when the salt geometry is simple. Variability in the salt interface geometry, especially rapid variability, will cause rapid defocusing of the raypaths, producing holes in the illumination patterns subsalt. These holes are dependent on the local geometry of the salt surface, and therefore can vary rapidly with the azimuths of the raypaths. This effect has been used to attempt to fill in the illumination holes by finding potential azimuths where the holes do not exist. This is the wide-azimuth revolution in seismic acquisition, which has led to a step change in the quality of subsalt images.

## MIGRATION ALGORITHMS

### A brief history of depth migration

As we discussed in the previous section, imaging near salt will require an accurate description of the physics of propagation. Hence, for most practical purposes, any migration method aimed at imaging the subsalt must be prestack and in depth domain; in other words, we shall only concern ourselves here with prestack depth migration. There are four main categories of such methods: Kirchhoff depth migration (KMIG), one-way wavefield extrapolation migration (WEM), RTM, and beam migration (BMIG). Although it is not the focus of this review to recount in detail the rich history of the development of these crucial tools, it is worthwhile to point out that, by the early 1980's, most of the main ideas behind these algorithms were already in-place. KMIG stems from 19th century scalar diffraction theory applied to sound waves, and was ported to the digital computer in the 1970's (see, for instance, French, 1974 and Schneider, 1978). This was also the time when Claerbout (1971) developed WEM theory and clarified the unifying principle of the imaging condition. RTM (Hemon, 1978, McMechan, 1983, Baysal 1983,

Whitmore 1983) and BMIG (Cerveny 1982, Costa 1989) were the last two pieces to fall into place.

These ideas ultimately came into widespread fruition in daily practice when the drill bit probed the subsalt in earnest (starting with the Exxon Mica well in 1990) and when computers could finally carry out the necessary tasks efficiently, ushering in the post-1990 era of modern subsalt imaging. For the first decade of this era, KMIG was the only widely available tool, although proprietary implementations of the other three methods were in limited use. Toward the end of that decade, shot profile WEM finally became commercially available and, during the first half of the 2000s, it became recognized as the leading technology for subsalt imaging. WEM's rapid adoption by the industry was mirrored by its equally rapid supplementation by RTM starting around 2005. Meanwhile, BMIG was being developed along diverging directions of performance or accuracy (Hill 1990, Sherwood 2008), gradually settling into the role as a preferred tool for situations where the need for computational speed is paramount, or where its nonlinear noise-attenuating side-effect is desired.

### The unifying imaging principle

Although these four methods appear very different in their operations, the imaging principle underlies them all. A reflection involves an incident wave and a scattered wave, commonly called the source and receiver wavefields. (We shall use the terms "reflect" and "scatter" loosely and interchangeably in this review.) The imaging condition states that the reflector is located where the source and receiver waves are nonvanishing at the same place and time. This is a consequence of the locality of interactions between waves and media (it's in fact microlocal as we will discuss later). This principle poses migration as the adjoint problem to the linear single-scattering approximation to wave propagation in inhomogeneous media, thereby breaking the task down into two simple steps: one must model two wavefields — the source and the receiver wave fields — and evaluate their zero-lag time-correlation at each subsurface point. These steps produce an image from one seismic record. Images from multiple records are summed to produce the stack image. The differences between the four methods result from the different ways in which they reconstruct, from recorded data, the two wavefields in the subsurface.

Under the single-scattering framework, transmission loss due to reflections and mode conversions is ignored. By treating migration as the adjoint of this linearized problem, we can, with little further loss of accuracy, make the assumptions of 1) an acoustic medium and 2) a smoothly varying density (in fact constant in most applications). These assumptions lead to a simplified wave equation that is the common starting point for all four migration methods. Each approach then proceeds to apply different approximations to this wave equation to develop its distinct algorithm. (After the developments outlined below, one can add anisotropy and absorption into the picture without any major change in the structure or characteristics of the algorithm.)

### Kirchhoff migration

#### Basics

In constant velocity KMIG, the two wavefields are constructed using the Kirchhoff or Rayleigh-Sommerfield diffraction integrals.

In the extension to prestack depth migration, traveltimes, and ideally, amplitude and phase shift data from dynamic ray tracing, are incorporated into the integral. This treatment relies on the separation of kinematics from amplitudes through the WKBJ asymptotic series expansion of the solution to the wave equation, and is accurate in the high-frequency limit. The first term of the series yields the eikonal equation, which determines the traveltimes. The second term provides first order approximation to the amplitude and phase shift of the wavefield. With the kinematics separated out, the time-correlation integral in the imaging condition can be evaluated in closed form, reducing it to a simple indexed look-up of samples from (properly filtered) input traces. As a result, KMIG maps each input time sample directly into the output image domain, forming a migration swing.

#### *Output flexibility*

This simplification yields a fast algorithm that is also very flexible, as it allows us to target the migration to image only a small subvolume or target line. It also allows us to keep track of the ray pairs involved in mapping each input time sample to the output image domain. This information enables the decomposition of the full stack image into common image gathers (CIGs) based on geometric attributes of the ray pair, such as surface offset, subsurface incidence angle, or direction of reflector normal. These advantages are shared with BMIG, but not with WEM or RTM, which treat the wavefields and lose ray attributes.

Another consequence of the direct sample-by-sample mapping nature of KMIG is the ease with which it can support the full bandwidth of the input data, a capability the other three methods can achieve only with increased computing cost. On the flip side of this advantage, proper antialiasing is more important in KMIG than in the other methods. Whereas the relatively low compute cost of KMIG was historically a reason for its widespread use, the ease with which KMIG generates CIGs in various domains and its ability to support high resolution images are the current reasons for its continued use.

#### *Image quality issues*

The same high-frequency approximation that gives KMIG its strengths also seriously limits its ability to handle situations involving large velocity variations. Foremost among the limitations is the inability to properly handle wavefield caustics, places where the wave front develops cusps and eventually crosses itself, resulting in multiple arrivals at many subsurface locations. In principle, the Kirchhoff integration can construct the wave front ray-by-ray, and there are in fact no caustics or multiple arrivals in ray-based coordinates. But in practice, to achieve reasonable computing performance, KMIG is typically implemented using traveltime tables sampled on a rectilinear grid, a domain in which it is very difficult to untangle caustics and handle multiple arrivals. Attempts to extend KMIG beyond the single-arrival assumption typically render its cost uncompetitive against the other migration methods.

Another limitation is the need to smooth the velocity model to approximate finite frequency propagation effects and reduce the amount of caustics. Due to this smoothing, even a best effort, dynamic ray traced, multiarrival KMIG cannot achieve the imaging quality that WEM and RTM can bring when truly sharp and rugose velocity boundaries are encountered as in subsalt imaging.

Another difficulty is the handling of amplitude divergences and phase shifts when ray tracing through wave front caustics. Many KMIG implementations make further sweeping approximations in this department, replacing dynamic ray tracing with purely kinematic methods that ignore phase shifts and yield no amplitude information. Approximate amplitudes from v-of-z approximations or from polygon representations of the wave fronts are then retrofitted to the solution. The strategy for postcaustic phase shifts is often to ignore it on the assumption that the phase shifted portion of the wave front is less likely to be retained after single-arrival ray path selection anyway. As result of these simplifications, most common KMIG products are of lower quality than even what a faithful single-arrival implementation can bring. A common expression of this problem is the proliferation of migration "swing" artifacts in poorly illuminated zones under or near salt bodies.

In current subsalt imaging practice, KMIG remains a useful tool for generating surface offset gathers for tomography, for target line migrations, and sometimes for high resolution image of the top salt, salt sutures, etc. For subsalt structural mapping, KMIG images are generally inferior to results from the other migrations. There is in general no good reason to use only a KMIG product for subsalt imaging.

## **Beam migration**

### *Basics*

One of the motivations for developing BMIG was to address the key weakness of KMIG. Huygens-Fresnel-Kirchhoff diffraction theory of waves treats any wavefield as a superposition of waves from point sources. KMIG's problem arises from the fact that the wave front from a point source necessarily propagates in all directions and easily folds onto itself when encountering even moderate velocity variations. In contrast, the beam decomposition treats any wavefield as a superposition of Gaussian beams, which are wave bundles that, even at their most focused location, are not fully localized points in space, but rather have a cross section with a Gaussian amplitude profile. This formulation abandons total spatial localization at  $t = 0$  for partial localization in both physical space and wave-number space for all time (i.e., optimal localization in phase space). This strategy yields optimal collimation of the beam, preventing it from spreading rapidly. This effect greatly reduces the volume of space the beam travels through, thereby reducing the likelihood for any one beam to develop caustics. With this treatment, even though each beam is modeled without considering caustics (by tracing only the central ray), the superposition of all beams can still adequately model most of the major caustics in the full wavefield, allowing BMIG to handle more complicated situations than KMIG. As a result, a high-effort BMIG can produce high quality images competitive with RTM in some cases.

Beam decomposition relies on dynamic ray tracing with Gaussian beam initial data (in principle, beam forming does not need to include ray tracing, it can be done purely in the time domain, although some beamforming applications do use ray tracing to form beams), which include beam center locations on the surface and the central ray's inclination (or direction ray parameters;  $p$ ). The initial data can be defined for each input data component only after the input seismic data have been decomposed through spatially windowed tau- $p$  transform into local dip components. Since it takes a pair of beams to form one image element, four

$p$  values are required to map one tau- $p$  component directly to one image component in 3D. The lower the dimension of the tau- $p$  transform actually used, the more the permissible combinations of dips one must sum over to fully migrate each tau- $p$  component. Hence, there is a trade off between initial dip picking effort and migration effort. It is typically when the migration is run multiple times that the performance advantage of BMIG emerges.

#### Data reduction

Tau- $p$  transformation does not automatically reduce the data volume, but the signal in unmigrated seismic data tends to be concentrated in a relatively small number of tau- $p$  components. This sparseness can be further enhanced when we perform along the tau dimension a parsimonious “wavelet” transform that approximates each  $p$  trace with a small number of wavelets. Many BMIG implementations only migrate a small portion of the wavelet- $p$  domain data points, through ranking by coherence or amplitude. This has the powerful side-effect of removing a large amount of random noise from the input data, although some weak diffraction tails can be lost as well, reducing fault resolution, for instance. This coherency promoting effect can be beneficial in some subsalt imaging situations. Often, a BMIG image is desired for this nonlinear aspect, which can lead to an alternative picture quite different from the other migration methods — the other methods all map every bit of input data into full migration operators (swings) in the image domain. However, the number of wavelet- $p$  domain data points needed to adequately represent the input data increases rapidly with maximum frequency, making retaining full high-frequency details difficult in BMIG.

Each beam carries geometric attributes for the central ray. Since the beam is partially localized around this ray, these geometric attributes can be considered approximate attributes for the whole beam, and can be used to decompose the full image into a rich variety of CIGs, retaining the flexibility of KMIG.

#### Image quality

Similar to KMIG, BMIG is reliant on velocity smoothing for ray tracing. Since only the beam central ray is traced, and there are far fewer beams used in a BMIG than rays in a KMIG, the smoothness requirement is even higher for BMIG, so as to ensure adequate sampling of the velocity model by the set of central rays.

The ability of BMIG to handle multiple arrivals means that in a high-effort BMIG implementation one can achieve an image quality which is superior to KMIG and which approaches that of WEM and RTM. With its added nonlinear S/N side-effects, BMIG can occasionally achieve better image of some subsalt features than RTM.

The complexity of BMIG also affords the practitioner an unusually large number of opportunities for making performance-enhancing approximations. The spatial window in the local tau- $p$  transform can be made large. The number of wavelet- $p$  components migrated can be kept small. Dynamic ray tracing can be replaced with purely kinematic ray tracing; wave front curvature can be roughly approximated. Narrow-azimuth assumptions can reduce the number of  $p$  combinations permissible for each underconstrained wavelet- $p$  component, etc. As a result, some BMIG implementations are tremendously fast. Typically, fast BMIG requires heavy smoothing of the velocity model due to the use of fewer and wider beams, and can yield very high S/N, albeit at the

expense of missing some weaker real events and smoothed-out structural details.

BMIG also has some ability to differentiate between primaries and multiples, but this capability is fairly limited when the dip information is incomplete, when there is velocity uncertainty, or when the velocity model is complex.

In current practice, BMIG is most often used for generating gathers for tomography, volumes for QC, and supplementary final volumes. Due to its nonlinear nature, a BMIG image should in general not be the only product for subsalt mapping.

### One-way wavefield extrapolation migration

In a departure from KMIG and BMIG, both of which use the asymptotic series to construct wavefields, WEM employs direct numerical solutions to the one-way wave equation, which only admits wave propagation in either up or down going directions. This method has no difficulty in constructing complicated wave front caustics, but cannot handle high-angle wave propagation, which is required for imaging steep dips. A serious drawback for imaging salt bodies, this problem is unique to WEM.

The one-way wave equation involves a square root of a partial differential operator, which is very difficult to evaluate in 3D inhomogeneous media, forcing us to make substantive numerical approximations that degrade the image beyond the basic one-way assumption. During the relatively brief prominence of WEM, a huge variety of numerical methods were developed to approximate this operator, but ultimately, only limited improvements in accuracy or performance can be achieved. Extending WEM to TTI anisotropy also proved more cumbersome than the other methods.

Other developments introduced cost-saving strategies that traded a small degradation in image quality for a large increase in compute efficiency. Delayed-shot migration decimates the input data in the source inline-coordinate slant stack ( $p_{SX}$ ) domain. Narrow-azimuth migration reduces the full double-square-root survey-sinking operation from 5D to 4D. These compromises tend to degrade the image quality of WEM further.

Efforts were also undertaken to extend WEM to handle steep dips and turning waves, either through tilted or curvilinear coordinate systems, or through storing evanescent energy for a second pass (Claerbout 1985, Hale 1992), but the limitations and complexities of these approaches were ultimately too much to overcome in the face of the simplicity and accuracy of RTM. As a consequence, the usage of WEM in subsalt imaging is becoming increasingly limited.

### Reverse time migration

#### Basics

The three preceding methods are characterized by the unique ways they approximate the wavefields involved in imaging, and by the unique limitations they suffer consequentially. In contrast, RTM implements the imaging principle in the most straightforward manner. It makes no further simplifying approximations beyond the common starting point, the unifying imaging principle outlined earlier. As a result, RTM is far more faithful in representing the full wave propagation phenomena than any of the other methods outlined above, namely the acoustic approximation with a smoothly varying or constant density. Artifacts in RTM images are typically not due to approximations RTM makes, but rather due to undesired

features in the fundamental imaging principle. We will expand on the imaging principle and its extensions in the next section.

#### *Early barriers to adoption*

Despite the directness of its approach, it was not until around 2005 that RTM was finally applied commercially on large 3D streamer data. The initial barrier was the high compute cost associated with RTM. This obstacle was overcome by the industry in short order. There are numerical corner cutting strategies that could speed up RTM, but quality is such a paramount goal for all RTM applications that the more common choice is to limit the maximum frequency of data migrated. Currently, RTM runs are typically limited to below 35 Hz for subsalt applications.

Aside from cost, another early reservation regarding RTM derives from the perception that RTM was somehow overly sensitive to velocity errors. However, since RTM is based on the same imaging principle as the other migration methods, its velocity sensitivity, in terms of imaging primary reflections, is not different. There was also the perception that RTM derives much of its power from imaging arrivals other than singly scattered primaries. In practice, the observations are that the strength of RTM stems mostly from its ability to construct the two wavefields accurately, and that, save for special cases, RTM primarily images single-scattering energy just like the other migration methods.

Another hurdle that RTM faced was the prevalence of back scattered artifacts in the raw correlation image output from RTM. These artifacts form when there are sharp velocity contrasts, such as top of salt, in the velocity model. When modeling the source wavefield using the wave equation, a reflected wave is scattered from the top salt. When this reflected wave in the source wavefield is correlated with the receiver wavefield constructed from the recorded trace at a receiver, an image of the first one or two Fresnel zones of the top salt reflection between the source and the receiver is formed. The full stack image thus contains the sum of such Fresnel zone images for all source receiver pairs. When the model is accurate, this artifact is a diffuse positive background bias in the image, and can be fairly easily removed by a Laplacian operator applied to the image or a mute applied to angle gathers. Alternative ways to practically remove these “artifacts” consist in modifying the imaging condition as we will discuss in the next section.

#### *Leading technology*

Once these hurdles were removed, RTM’s wide adoption was swift. It was also quickly extended to handle VTI and TTI anisotropy, all while staying with pseudoscalar wave equations. RTM is able to deliver on its promise of high quality imaging, producing better subsalt images than the other methods in most situations. Currently, most workers in the subsalt imaging field consider RTM the leading migration technique and the preferred product in most situations.

#### *Angle gathers*

One important development during WEM’s heyday was the generation of angle gathers. These developments continued as RTM became more common, as the techniques are equally applicable to RTM.

We have alluded to the fact that the imaging principle is micro-local, i.e., point-like, yet with internal structure. This internal

structure is the angle and azimuth dependent reflectivity — the scattering matrix — and it can be analyzed if we take the local spatial Fourier Transform (FT) of the incident and reflected wavefields and apply the imaging condition to each pair of incident and reflected local plane waves. Local plane waves carry geometric attributes, allowing us to measure the incidence angle of the component of the reflection represented by a local plane wave pair. The image contribution from each plane wave pair can be binned according to the associated angle and azimuth, yielding angle gathers (de Bruin 1990). This is computationally very intensive, necessitating Fourier domain data high-grading (decimation), which can actually have beneficial artifact-removing side-effects (Xu 2010). The use of high-graded local plane waves is analogous to the situation in BMIG.

With the FT before the imaging condition, the latter no longer appears strictly local. This leads to the realization that the imaging condition can be extended beyond strictly “same place and time” and include crosscorrelations of the incident wave at point A with the scattered wave at point B, with A and B offset from each other laterally and/or vertically. The cross-correlation can also be evaluated at nonzero time lags. The angle dependent information of the reflection event is preserved in the extended images, which can be converted into angle gathers under 2D (Rickett 2002) or 3D assumptions. We will expand on these extended imaging conditions in the next section.

Other workers use the vector nature of the wavefield to derive angle attributes. The solution to the scalar wave equation can be considered the P-wave potential, from which particle velocity and Poynting vectors can be computed. Emerging techniques propose to form angle gathers based on local instantaneous geometric attributes derived from these vector fields (Zhang, 2011).

### **True amplitude**

Although current subsalt imaging efforts are still primarily geared toward producing a good structural picture of the reservoir and the fault system, it is often speculated that attempts at extracting amplitude-based attributes from the subsalt section will become more common. In this context, the basic requirement is that the migration be amplitude preserving, so that amplitude anomalies can be resolved from the background statistically. A more quantitative approach is to make the migration “true amplitude,” which is to pose the migration procedure not merely as an adjoint problem, but as an inverse problem.

One approach is to seek a solution to the inverse problem using the WKB high-frequency limit, thereby deriving various migration weights in the KMIG and BMIG cases (Beylkin, 1985, Cohen, 1986). These weights can be converted back to partial differential operators and modifications to initial and/or boundary conditions for WEM and RTM cases (Zhang, 2002). To find closed form formulations, this approach typically relies on v-of-z assumptions. In other words, illumination variations are ignored.

An ambitious approach is to employ inversion techniques to the finite frequency (linearized) forward problem, converting the migration procedure into migration deconvolution or inversion. Illumination effects are then accounted for. These methods are typically compute-intensive, and tend toward ill-posedness in areas of low illumination. Illumination gaps lead to degeneracies in the forward modeling operator — i.e., different models can produce the same seismic data — and require the introduction of a priori constraints

in the inversion. A priori geological/structural constraints predispose the image toward preconceptions.

It is difficult to define true amplitude for the full stack because the stack is an average of measurements of nonidentical attributes. What we desire most often in a stack is high S/N, which is a statistical goal. This goal is expressedly not the inversion goal of true amplitude treatments. As a result, true amplitude treatments do not optimize S/N of the stack.

In a majority of situations, to extract subsalt amplitude-based attributes not dominated by overburden, effects will require much more complete sampling of the wavefield during data acquisition than the industry is currently practicing.

## A DETAILED REVIEW OF IMAGING CONDITIONS

In the previous section we have given a historical context to imaging, and described qualitatively the four main methods of prestack depth migrations that are pertinent to subsalt imaging. We were rather cursory in our reviews of these methods. In this section, we expand a bit more on the imaging methods, paying particular attention to the various implementations of the imaging principle. It will be seen that this seemingly trivial principle gives a rich set of diagnostic tools that are crucial to unravel the subsalt problem and other difficult imaging situations.

Prestack depth migration is the most physically accurate imaging technique and it serves three main purposes: 1) to produce a structural image of the earth; 2) to estimate migration velocity; and 3) to render an image whose amplitudes or other attributes provide an interpreter access to rock or fluid properties. As discussed earlier, the existing migration methods can be classified into two major groups: ray-based methods such as KMIG and BMIG, and wave equation-based methods such as WEM and RTM.

A seismic migration algorithm includes the computation of source and receiver wavefields and construction of the image by applying a proper imaging condition. These two steps are explicitly stated in the wave equation-based migration methods, but they are implicitly represented in ray-based methods. The imaging principle has typically taken advantage of the convolutional model of seismic reflection. A KMIG image formulated in the time domain gives the image  $I(x)$  at the image point location  $x$  as:

$$I(x) = \int d\Gamma \int A(x; r, s) \frac{\partial d(t; r, s)}{\partial t} \delta[t - (\tau_r + \tau_s)] dt \quad (1)$$

Depending on the summation geometry,  $\Gamma$  represents receiver coordinates (common shot migration), offset (common midpoint migration) or midpoint (common offset migration);  $A(x; r, s)$  is the amplitude scale factor,  $d(t; r, s)$  is the recorded data at receiver position  $r$  from a source at  $s$ , and  $\tau_r = \tau(x, r)$ ,  $\tau_s = \tau(x, s)$  are the travel times from receiver  $r$  and source  $s$  to the imaging point,  $x$ , respectively.

One-way wave equation-based migration methods like WEM utilize the paraxial approximation to the wave equation to extrapolate the wavefields from one depth to another for each frequency component. RTM on the other hand, directly solves the acoustic two-way wave equation for wavefield propagation. The image is typically constructed by taking the zero-lag crosscorrelation of the extrapolated source and receiver wavefields, i.e., the “same time same place” imaging principle (Claerbout, 1985). As WEM migration is usually implemented in the spatial-frequency domain, the

image is simply represented as the integration over frequency for the product of the upgoing receiver wavefield  $R(\omega, x)$  with the conjugate of the downgoing source wavefield  $S(\omega, x)$ , i.e.,

$$I(x) = \int \bar{S}(\omega, x) R(\omega, x) d\omega. \quad (2)$$

For RTM, which is typically implemented in time domain equation 2 becomes the integration over time of the product of the source and receiver wavefields, i.e.,

$$I(x) = \int S(t, x) R(t, x) dt. \quad (3)$$

These correlations, which represent the same time same place physical requirement, provide correct structural images and are efficient to implement. In Kirchhoff and one-way wave equation migration, this imaging condition has been widely applied. However, in RTM, the imaging condition expressed in equation 3 produces significant amounts of large-amplitude, low frequency noise at sharp interfaces that contaminate the image (see Figure 1). We discussed earlier a reason for this phenomenon. Another way to look at it is that the full wave equation used in RTM properly simulates wave propagation in all directions including both reflections and transmissions, and consequently the forward extrapolated source and backward extrapolated receiver wavefields have the same wavepaths. The crosscorrelation of these two wavefields then produces an amplitude not only at a reflection point, but also at all nonreflecting points along the entire wave path, which builds up the low frequency artifacts when the integration over time is applied. This noise has been one of the major concerns for RTM and can be handled in a variety of pragmatic ways, such as a Laplacian operator filter of the image, or a mute applied to the angle gathers. Another, less ad hoc way to attenuate this noise is to modify the way that the imaging principle is applied, so that only a true reflection produces an image. This new imaging condition requires the local decomposition of the full wavefields into their one-way components along some specific direction, such that the properly decomposed components will only correlate at a reflector (Liu et al., 2011). Figure 2 shows the image obtained with this new imaging condition. Comparing to Figure 1, the low frequency artifacts have been successfully removed as expected from physical arguments. Since these low frequency contaminants are much more prominent at strong reflecting interfaces it is critical to use such techniques for imaging subsalt.

## Imaging condition for true amplitude migration

The correlation-based imaging conditions in equations 1–3 produce the correct kinematics (“same time, same place”). However, they do not produce the true amplitudes, which can be important for properly extracting rock properties. True amplitude KMIG is, as stated earlier, essentially an inversion that produces not only an image of the earth, but also the correct amplitude that is proportional to the reflection coefficient at the image point (Bleistein, 1987)

$$I(x) = \iint d^2\xi \frac{|h(x, \xi)|}{A_s A_r |\nabla \tau_s + \nabla \tau_r|} \frac{\partial d(t; r, s)}{\partial t} \delta[t - (\tau_r + \tau_s)]. \quad (4)$$

Though equation 4 has the same basic form as equation 1, it includes the factors that affect the amplitude namely,  $A_s = A(x, s)$  and  $A_r = A(x, r)$  which are the WKBJ (or ray theoretic) amplitudes of the Green's function with the source at  $s$  or  $r$  and the observation point  $x$ , respectively.  $h(x, \xi)$  is the so-called Beylkin determinant.

A true amplitude migration requires proper handling of both the wavefield propagation and an appropriate implementation of the imaging principle. The original one-way wave equation, which is the paraxial approximation to the acoustic wave equation, does not preserve the dynamic information of the wavefield propagation, as it does not properly handle the geometrical spreading. Zhang et al. (2005) proposed a new one-way wave equation that takes care of the propagation effect. To produce a true amplitude image, a deconvolution-type imaging condition has to be applied instead of the correlation-based formula (Kelly and Ren, 2004, Zhang et al., 2005). For a one-way wave equation, it is implemented as the ratio of the receiver and source wavefields at each frequency component,

$$I(x) = \int \frac{R(\omega, x)}{S(\omega, x)} d\omega \quad (5)$$

This imaging condition still enforces the same time same place principle, but it normalizes the amplitudes to the incident flux. However, as written, this imaging condition suffers from numerical stability issues when the denominator is small. To circumvent this problem, the deconvolution imaging condition is often modified to

$$I(x) = \frac{\int \bar{S}(\omega, x) R(\omega, x) d\omega}{\int \bar{S}(\omega, x) S(\omega, x) d\omega + \epsilon}. \quad (6)$$

The image in equation 6 is often referred to as a source illumination corrected image as the denominator essentially defines the energy of the source wavefield. Here,  $\epsilon$  is a small undefined and arbitrary damping factor.

Even though there is no direct extension of the deconvolution imaging condition for RTM, which is normally implemented in time domain, an extension similar to equation (6) is often applied to compensate for the illumination effect, i.e., the incident energy,

$$I(x) = \frac{\int S(t, x) R(t, x) dt}{\int |S(t, x)|^2 dt + \epsilon}. \quad (7)$$

The correlation-based imaging condition in equations 2 and 3 do not generally produce the correct amplitude in the stacked image, however, it can produce true amplitude angle gathers for both one-way wave equation and RTM (Zhang et al., 2007, Zhang and Sun, 2009).

### Migration gathers

One of the main applications of migration is to derive a migration velocity model, which is computed by evaluating the quality of the flatness or focusing of image gathers, which quantitatively links the image mismatch to velocity error, assuming that correct velocity model yields a flat common image gather or properly focused gathers. The flatness of the gathers is a sort of imaging principle as well, which expresses the fact that every offset must yield the same structural image, as each offset is an independent experiment. The image gathers can be broadly classified as offset gathers and angle gathers.

It is straightforward to produce surface offset gathers in KMIG, which have been the most widely used in ray-based tomography inversion for a velocity model. However, a typical image gather in the offset domain shows contamination from artifacts in a complex region due to the nonuniqueness of the image when the imaging condition is applied in the common offset domain (Nolan and Symes, 1996). Common diffraction-angle gathers, as proposed by Xu et al. (2001), do not suffer from these noises and provide the required information for carrying out a migration velocity and Amplitude versus Angle (AVA) analysis. Figure 3 shows some comparison of offset and diffraction-angle gathers, which clearly demonstrate the difference of noise level in the two types of gathers.

In wave equation-based migration, common imaging gathers with respect to surface offset are not computationally efficient. To take advantage of wave equation migration for migration velocity analysis, common image point gathers are often constructed as a function of space ( $h$ ) and time-lag ( $\tau$ ) in the subsurface near the image point. These extended crosscorrelations "probe" the accuracy of the same time same place principle in the neighborhood of an image point. Physically the location around the image point

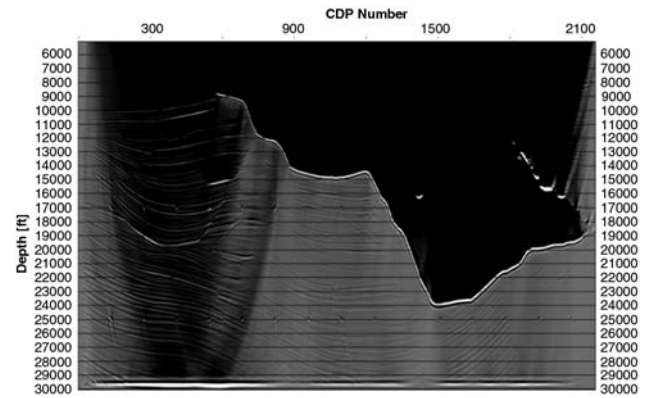


Figure 1. A RTM of the entire 2D line of the Sigsbee model using the crosscorrelation imaging condition of equation 2. Note the large low-frequency noise (black) component of the image.

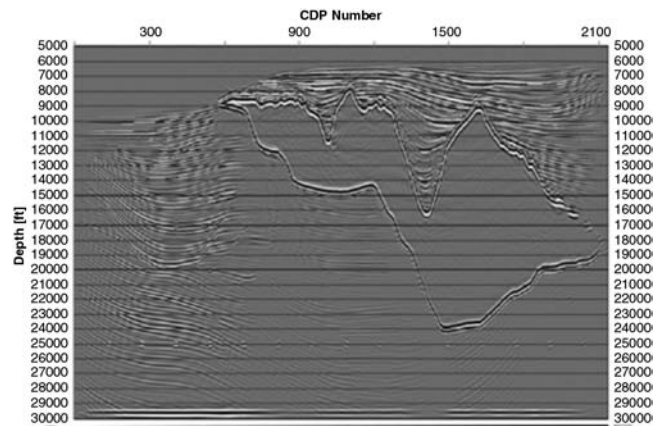


Figure 2. RTM of the BP data for the Sigsbee line using the new imaging condition of Liu et al. (2011).

where the crosscorrelation is maximized and yields an estimate of the inaccuracy of the velocity model. For one-way wave equation migration, this extended imaging condition is represented in the frequency domain as,

$$I(x, h, \tau) = \sum_{\text{shot}} \int e^{i2\omega\tau} \bar{S}(\omega, x-h) R(\omega, x+h) d\omega \quad (8)$$

The time domain representation of the extended imaging condition for RTM is formulated as

$$I(x, h, \tau) = \sum_{\text{shot}} \int S(t-\tau, x-h) R(t+\tau, x+h) dt \quad (9)$$

With these extended imaging conditions, the correct velocity model will produce image gathers that focus at zero-lag at every delayed direction. Figure 4 shows the comparison of the imaging gathers for different velocities. The semblance principle in wave equation migration velocity analysis relates the focusing lag quantitatively to the velocity error.

In equations 8 and 9, the extended image is constructed with shifts in both space and time. Common image gathers can be constructed having either spatial or temporal lag and both can be converted to angle gathers. In two dimensions, the angle gathers can be computed by a slant stack from the spatially shifted gathers as

$$\tan \theta = \frac{|k_h|}{|k_m|}. \quad (10)$$

Here,  $m$  is the imaging position,  $k_m$  and  $k_h$  are the wavenumbers for the image point and subsurface offset, respectively. The same angle gathers can also be computed from the time-delayed image gathers as (Sava and Fomel, 2006),

$$\cos^2 \theta = \frac{\tau_x^2 + \tau_y^2 + \tau_z^2}{s^2(x)} \quad (11)$$

Where,  $\tau_x, \tau_y, \tau_z$  are the partial derivatives of the delay time with respect to  $x, y,$  and  $z,$  respectively, and  $s(x)$  is the slowness.

Figures 5 and 6 show the angle gathers computed from spatially shifted image gathers and time shifted image gathers for the same imaging point, respectively (these corresponds to Figures 9 and 10 in Sava and Fomel, 2006).

However, the angles defined in both equation 10 and 11 are opening angles only, neither of them has azimuthal information, which can be important for taking full advantage of wide-azimuth data and extract from it azimuthally dependent attributes such as anisotropic parameters. Using a local plane wave decomposition of the source and receiver wavefields in RTM, Xu et al. (2010) derived a 3D angle domain common imaging gather, which gives both azimuth angle ( $\varphi$ ) and dip angle ( $\theta$ ) at subsurface imaging points,

$$\cos \theta = \frac{k \cdot k_r}{|k||k_r|},$$

$$\text{and } \sin \varphi = \frac{(k_s \times k_r) \cdot (k \times n_x \times k)}{|k_s \times k_r||k \times n_x||k|}. \quad (12)$$

Where,  $k_s, k_r$  are the wavenumber for source and receiver coordinates, respectively,  $k = k_s + k_r,$   $n_x = (1, 0, 0)$  is a unit vector. Figure 9 shows an example of this 3D angle domain imaging gathers for a wide-azimuth data set. The differences among the angle gathers at different

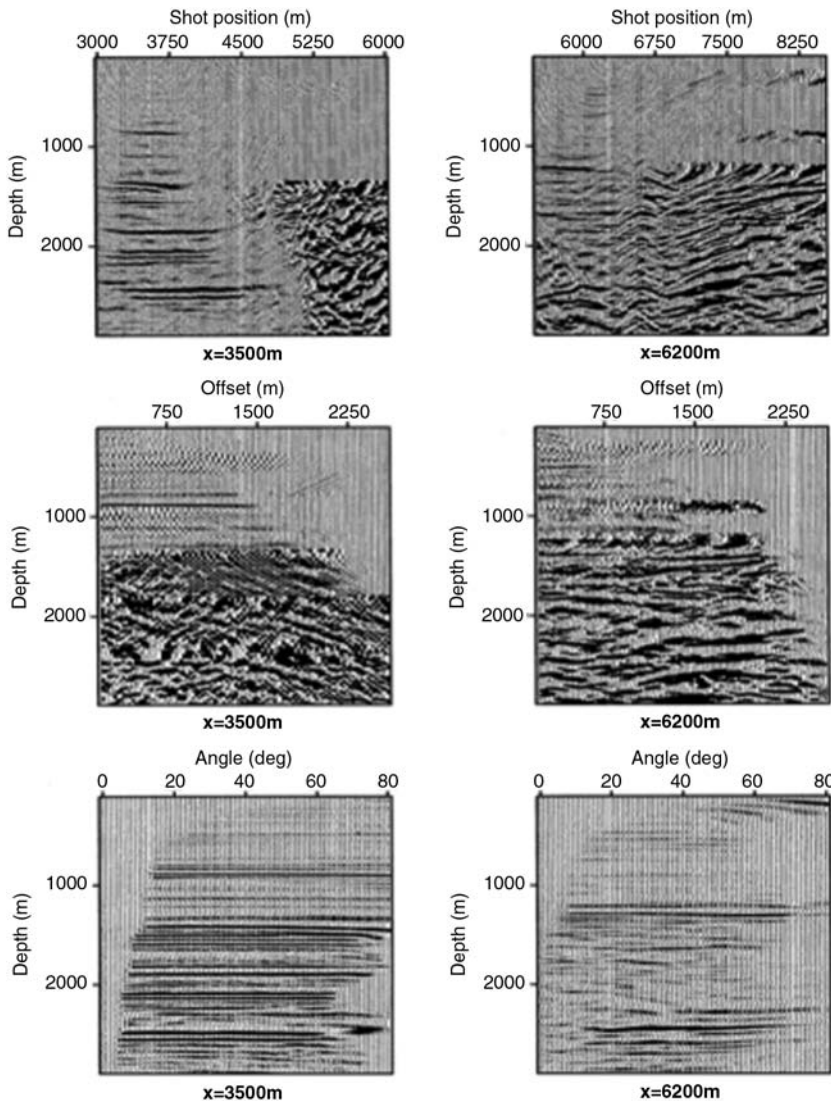


Figure 3. Common image gathers in the shot (top), offset (middle), and angle (bottom) domains in the complex and non complex part of the Marmousi model (Figure 17 of Xu et al., 2001).

azimuths clearly indicate the azimuthal variations of the reflection. (Xu et al., 2010 Figure 3).

We hope that this brief review has given the reader a glimpse into the richness of the imaging principle. The (micro) local nature of this principle, when fully implemented, gives rise to a wide array of tools to evaluate the correctness of the migration velocity and other kinematic and dynamic variables locally in image space. This power is fully utilized to produce the best images in subsalt imaging.

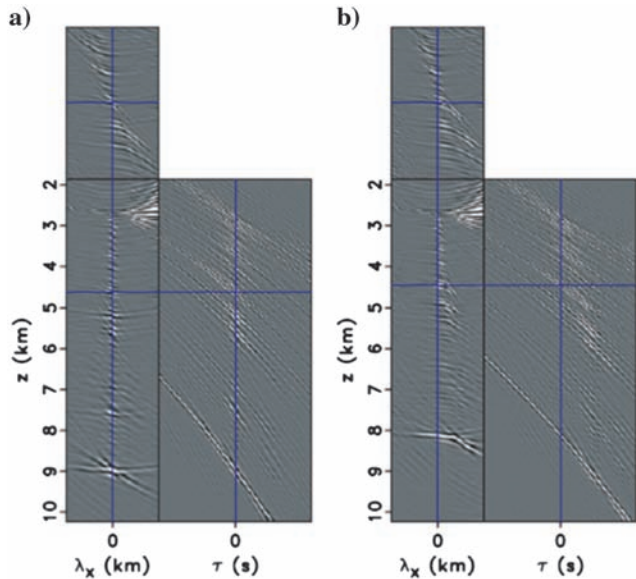


Figure 4. A space and time-lag common image gather for the Sigsbee model with the correct velocity (a) and an incorrect low velocity (b). This corresponds to Figure 5 of Sava and Vasconcelos (2011).

## VELOCITY MODEL BUILDING AND UPDATE

### Velocity model building in salt provinces

Salt bodies pose significant challenges for velocity model building due to the usually large velocity contrasts with the surrounding rocks and the irregularity of their surfaces (sometimes due to dissolution collapse features). These irregularities scatter and refract the incident sound waves to such an extent that the underlying structures are often poorly illuminated. The velocity distribution around a salt body can be further influenced by buoyancy forces, giving rise to significant deviations in velocity from any expected depth-of-burial trends, and by various chemical reactions with the salts and associated minerals.

In this section of the review, we'll first consider establishing the geometry and velocity distribution of the salt geobody, and then consider how to update velocity below the salt geobody.

### Salt geobody geometry

Current industrial practice for building a velocity model incorporating a salt body would involve something along the following lines (e.g. Jones, 2010):

- 1) migrate with the overlying and/or adjacent sediment velocity (which has been previously determined with conventional tomographic techniques),
- 2) pick the top salt and nonrecumbent (i.e., nonoverhanging) salt flanks outboard of the top canopy,
- 3) update the model to include the salt velocity, "flooding" the model below the top salt, but perhaps bounded by the salt flanks (the salt velocity need not be a constant, but could involve inclusions using "dirty salt" update techniques, e.g. Haugen et al., 2008),
- 4) perform a new migration with this updated model,
- 5) pick the base salt and any recumbent salt walls,
- 6) update the model geometry to incorporate the salt body,

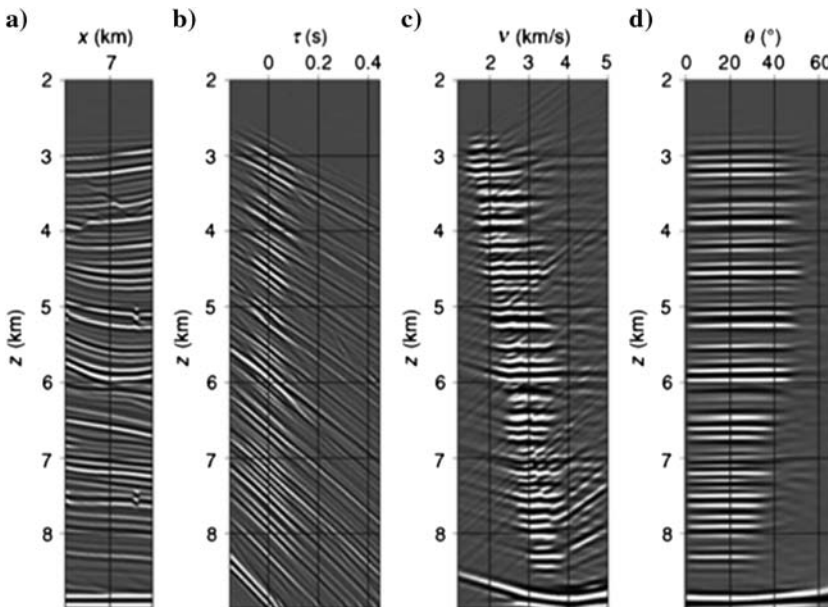


Figure 5. Time-shift Imaging condition gathers from the Sigsbee model. The panels depict (a) the image (b) the time-shift gather (c) the slant-stacked time-shift gather and (d) the angle gather (from Sava and Fomel 2006, Figure 9)

- 7) perform a new migration with this updated model,
- 8) repeat steps 5 to 7 as required for all recumbence's (i.e., we may have several overhanging salt features giving a "Christmas tree" appearance),
- 9) insert sediment velocity below the salt,
- 10) update subsalt sediment velocity.

These steps are demonstrated in the following figures using a 2D salt model (Figure 8a) and synthetic data (courtesy of BP, [Billette and Brandsberg-Dahl, 2005](#)). The process commences with an estimate of the background velocity field, omitting the complex salt geobody (Figure 8b), and a migration is produced with this "sediment only" model (Figure 8c). The top of the salt, and any deeper nonoverhanging flanks are picked from this image, just above the

thick dashed lines indicated in Figure 10c. Salt velocity is inserted into the model below the positions of the top salt pick and the deeper nonoverhanging salt flank picks, and extended vertically ("flooded") below these picks as appropriate (Figure 10d). A new migration is produced and the base of the salt body picked where visible (Figure 8e). Sometimes on real data, the base salt is illuminated by converted mode arrivals, so migrating with the salt P-wave velocity replaced with the corresponding S-wave salt velocity can occasionally produce an interpretable image of the base salt. This can be possible as the converted rays follow a different raypath, hence provide different illumination (e.g., [Lewis, 2006](#)). Combining the picks from the top, flanks, and base of the salt permits construction of a geobody which is now inserted into the model (Figure 8f). Migrating with this model produces the image shown in

Figure 6. Space-shift imaging condition gathers for the Sigsbee model data. The panels depict (a) the image (b) the space shift gather (c) the slant-stacked space shift gather and (d) the angle gather (from [Sava and Fomel 2006](#), Figure 9).

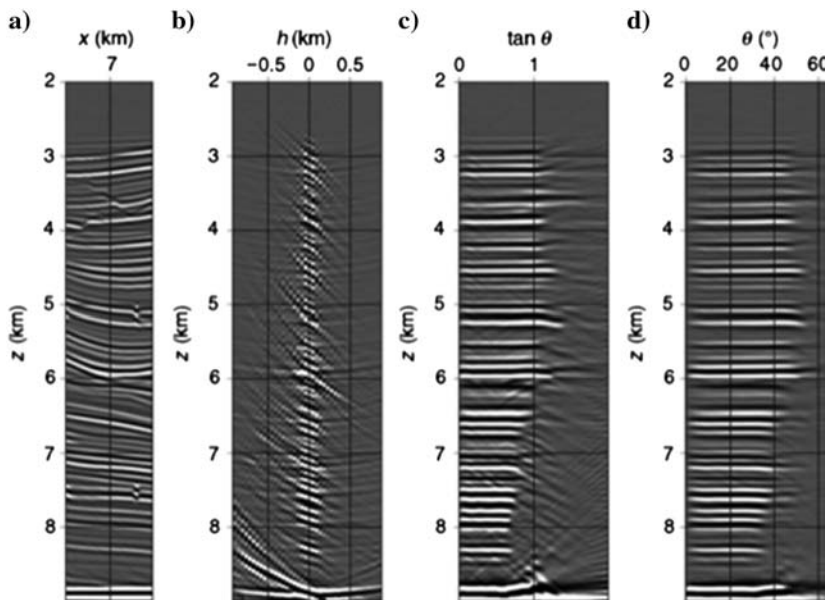


Figure 7. A WAZ data application. The vertical axis is depth. Left panel shows the stack image of a TTI RTM. The right panel shows angle gathers at a location near the middle of the stacked image versus reflection angle for six azimuth angles. From left to right, the azimuth angle is 0°, 30°, 60°, 90°, 120°, and 150°.

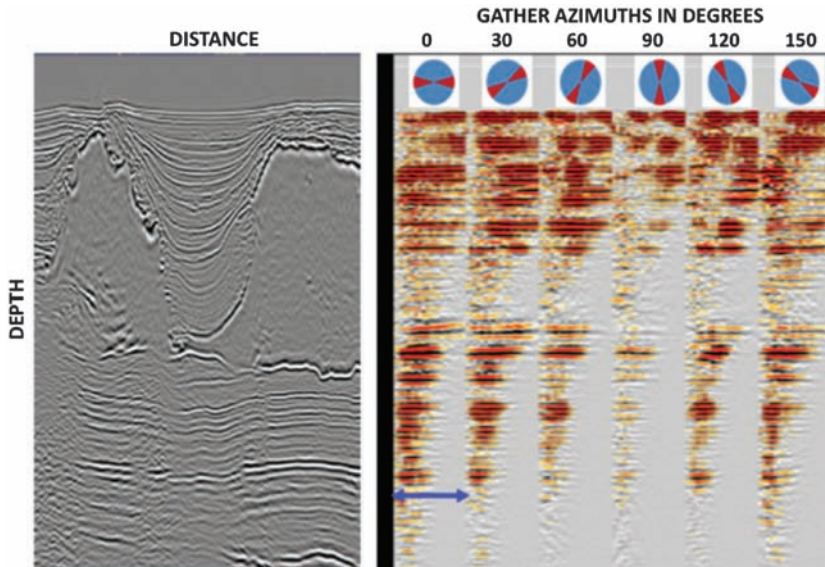


Figure 8g. For comparison, the correct model and image are shown in Figures 8h and 8i. The migration used for this example was RTM.

However, when a large-velocity-contrast geobody is present, the significant lateral velocity change can cause this more conventional top-down layer stripping velocity model building methodology to fail. For example, in a KMIG, where we compute the traveltimes independently from both the source and receiver locations down to the subsurface image point, and then use these travel times to build the image, the downgoing raypath near the edge of a salt body might be in sediment and the upcoming path in salt. Hence in this case if we perform a “velocity-flood” with sediment velocity, the upcoming raypath will be incorrectly dealt with (e.g. Anderson and Marcinkovich, 2005).

In addition, various salt geobody shapes could be assessed using scanning techniques, producing a suite of migrations and/or CRP gathers for a range of perturbed velocity models (Audebert & Diet, 1996; Jones et al., 1998, Jones et al., 2000; Wang et al., 2008). This approach is especially powerful for noisy data, and below salt where we have little angular distribution in the angle gathers (discussed further in the next part of this section), although scanning techniques are inherently subjective in that choosing the “optimal” result is usually interpretational. In other words, there is not usually an objective criterion for selecting the “best” member of the scan (although some attempts to improve on this have been made, e.g. Biondi, 2011).

Furthermore, the type of migration algorithm used must be considered: ray-based schemes are not usually best suited for imaging

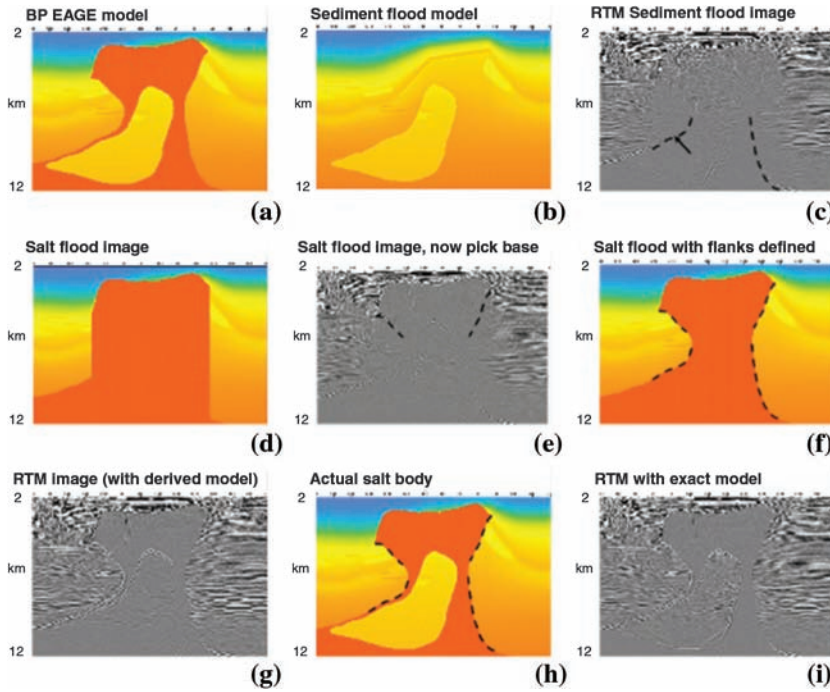


Figure 8. (a) Portion of the BP 2D sale model used to generate synthetic data. (b) The salt body has been removed to create a “sediment only” model for commencement of a salt model building workflow. (c) Migration using the sediment only velocity field produces an image from which the top salt and some salt flank horizons can be picked. (d) The salt picks are inserted into the velocity model, and values of salt velocity “flooded” vertically below the picked top and flank salt boundaries. (e) From the salt flood migration, the base salt horizon is picked. (f) The salt body geometry is updated based on the available picks to create the salt geobody. (g) Migration using the derived salt model. (h) Correct BP salt for comparison. (i) Migration using the correct salt model for comparison.

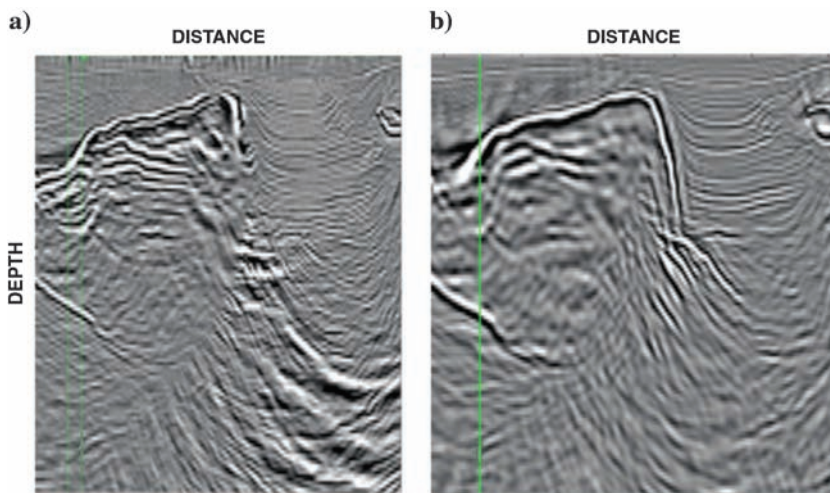


Figure 9. a) WEM image of deep water West African salt body. The steep right flank of the body is not imaged, and the consequentially mispositioned energy appears elsewhere in the image as ‘migration noise’; b) RTM image- the steep salt flank is now imaged, profiting from correctly exploiting double bounce arrivals.

very rugose surfaces with large lateral velocity contrasts, due to the smoothing of raypaths required for stable ray-tracing, and the inherent limitations of the high-frequency approximation, when the wavelength of the incident sound waves are of similar scale length to the velocity anomaly encountered (Pratt, 2003). Hence a WEM of RTM algorithm might be preferred for picking rough top salt geometries. Also, below salt, a Kirchhoff scheme would not be used as multipathing is expected, hence wavefield continuation (or beam) algorithms tend to be used.

There are many excellent case studies in the literature dealing with such salt body problems, especially from the Gulf of Mexico, where much subsalt exploration has occurred in recent years (e.g. Albertin et al., 1998a, b; Albertin et al., 2001; Kapoor et al., 2007, 2008; Lewis, 2009). More recently, exploration offshore west Africa, in the deep water regions, has also encountered salt related imaging challenges (e.g. Sexton et al., 2009). For example, Figure 9 compares a deep water West African salt body imaged with two-way RTM and one-way WEM (using split step Fourier plus interpolation), demonstrating the importance of the algorithm being used to visualize the salt body. Often it is not the dip-limitation of the algorithm that prevents us from imaging steep salt flanks, but simply the fact that one-way raypaths from a steeply dipping reflector do not return to the surface (Jones, 2008). A two-way ray propagator such as RTM, is required for such geometries so as to capture double bounce arrivals (turning-ray energy can also achieve this if a significant vertical velocity gradient exists).

### Subsalt Velocity Update

There are two different contemporary approaches for subsalt sediment velocity update: Subsalt tomography based on residual moveout picks in common image point gathers (Woodward et al., 2008; Wang et al., 2008); and subsalt velocity update using migration scanning techniques (Wang et al., 2004, 2006, 2009; Jiao et al., 2006; Ritter 2010). In this section, we will briefly describe these alternative subsalt velocity model building techniques, and use real data examples to illustrate the effectiveness of some of the approaches.

### Subsalt tomography

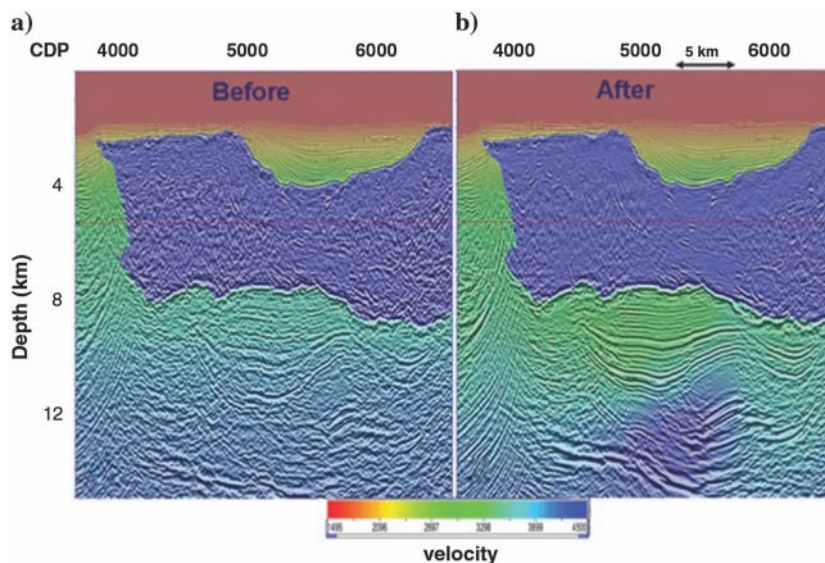
Woodward et al. (2008) provided a good review of the evolution of seismic tomography for velocity model building. Similar to sediment tomography, the input for subsalt tomography are residual moveout picks which are automatically performed on the common image point gathers. Both Kirchhoff-based surface offset gathers as well as angle gathers using WEM or RTM (Sava and Fomel, 2003; Fomel, 2004, Xue et al., 2010) are routinely used in production for subsalt tomography.

There are a few challenges for subsalt tomography. First, typically the S/N is poor in subsalt areas; second, there is limited angle coverage in subsalt areas, especially for deeper subsalt areas. To increase the robustness of automatic picking for residual moveout in common image point gathers, good gather preconditioning is critical. In reasonably good signal to noise ratio areas, subsalt tomography is an effective tool for updating subsalt sediment velocity models resulting in improved subsalt images.

Figure 10 shows a real data example of how 3D subsalt tomography can improve a subsalt velocity model. On the left side of the Figure is the WEM image overlaid with the velocity model before the subsalt tomography, and the right side of the figure shows the comparison after subsalt tomography. After subsalt tomography, the subsalt image is significantly improved with better focused and more coherent subsalt events. The subsalt sediment velocity is reduced by about 10% right below the base of salt, and in the deeper portion, the velocity is increased, which makes good geological sense and is consistent with the interpreted carbonate layers.

In addition to the challenges already mentioned with subsalt tomography, there is also the theoretical consideration of using residual velocity error picked from WEM or RTM gathers as input to a ray-based tomography, unless we restrict the raypaths used in the tomographic back propagation so as to avoid salt complexity. However, in practice the method is still of great use. More recent developments in full waveform inversion (FWI) and waveform tomography offer further potential to refine salt geometry using full waveform (non ray-based) techniques (e.g. Vigh, et al., 2010), thereby avoiding the limitations of ray theoretical approaches.

Figure 10. a) WEM image before subsalt tomography; b) WEM image after subsalt tomography.



**Subsalt velocity perturbation scans**

In some noisy subsalt areas where common image gathers may not provide reliable residual moveout picks, or for some deep subsalt areas where there is not enough angle coverage, we may have to rely on the more brute force approaches of scanning techniques (Audebert et al., 1996; Jones et al., 1998). One common subsalt scanning technique is called velocity perturbation scanning (Jones et al., 2000; Wang et al., 2004, 2006; Jiao et al., 2006). In this approach, the currently available subsalt sediment velocity is used as a reference velocity model or called the 100% velocity model. Then a set of scaled velocity models are produced and migrations are performed for each of these scaled velocity models. Typically seven to nine scans are produced and the scan images are compared and picked to update the subsalt velocity model.

Figures 11 and 12 show an example from a Gulf of Mexico 3D project which illustrates the effectiveness of subsalt velocity update based on velocity perturbation scans (Wang et al., 2008). Figure 11b shows the updated velocity after the velocity perturbation scans. Compared with the initial velocity model (Figure 11a), there was about 20% decrease in velocity right below the salt body on the left side the model. Figure 12b shows the new 3D prestack migrated image using the updated velocity model after the subsalt velocity perturbation scans. Clearly, after the subsalt scans velocity update, not only have we significantly improved the subsalt image focusing, but the target zone is also more interpretable. As shown in Figure 12a, the original subsalt image shows conflicting crossing events in the target zones. The new image also ties the well better, and more accurately shows the dip of the bedding layers.

Velocity perturbation scans can also be used to update other complex geological areas. Ritter reported a case history where velocity

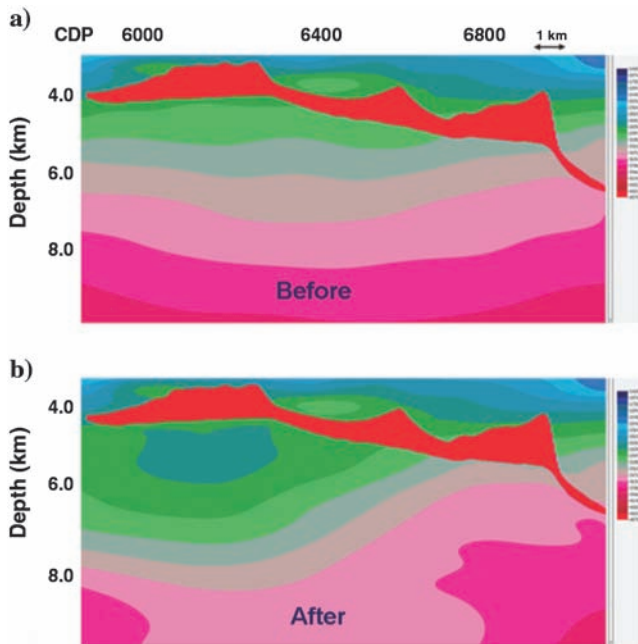


Figure 11. (a) Velocity model before velocity perturbation scans; (b) Velocity model after velocity perturbation scans.

perturbation scans were effectively used to improve the velocity model for a mega suture between two large salt sheets (Figure 13). Shown by Figure 13 and Figure 14a, on either side, beneath the two salt sheets, the image is very good. It is within the suture zone where the subsalt image disappears or is distorted and not aligned with either side. Several scenario tests showed that salt geometry changes were not the only answer. A low velocity region was defined (Figure 13), and slower sediment velocities were scanned through

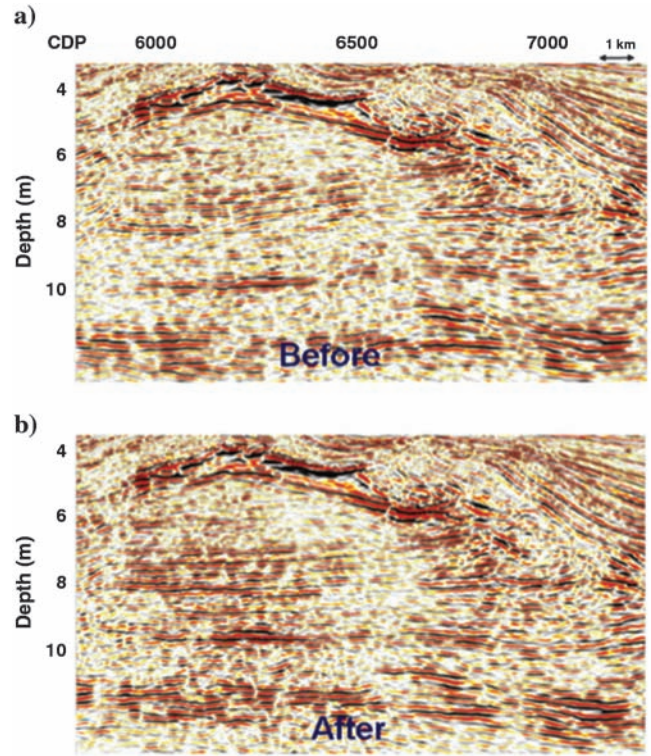


Figure 12. (a) WEM image before velocity perturbation scans; (b) WEM image after velocity perturbation scans.

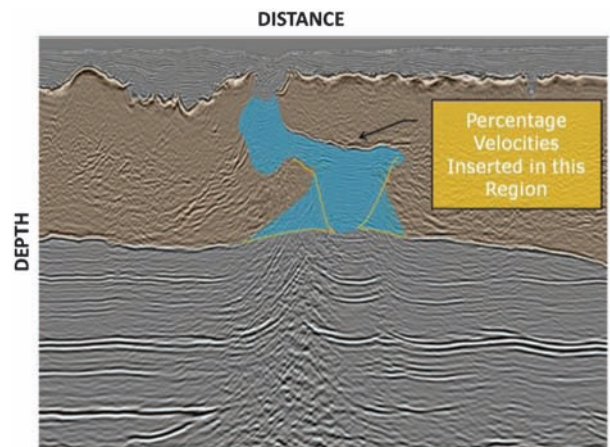


Figure 13. Velocity perturbation scans applied to velocity model between salt bodies.

this region. A percentage velocity was found that allowed the marker events below the suture zone to be consistent with the surrounding sediment. This allowed a more geologically reasonable salt interpretation to be put in-place. Figure 14b is the migration image after the velocity perturbation scans, in which the subsalt continuity has been greatly improved.

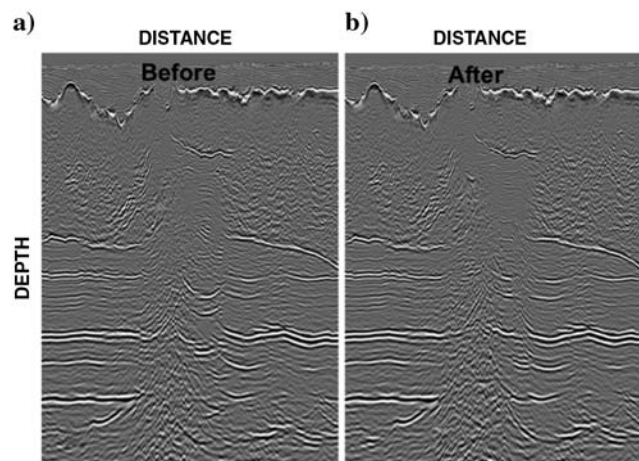


Figure 14. (a) RTM image before velocity perturbation scans; (b) RTM image after velocity perturbation scans.

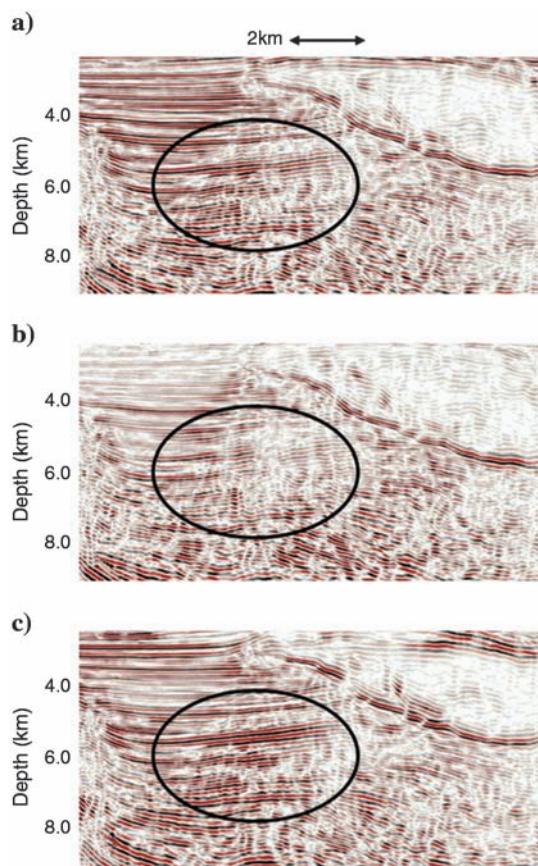


Figure 15. An example of DIT-scan panels with delayed imaging time: (a) 0 ms; (b) +100 ms; (c) -100 ms.

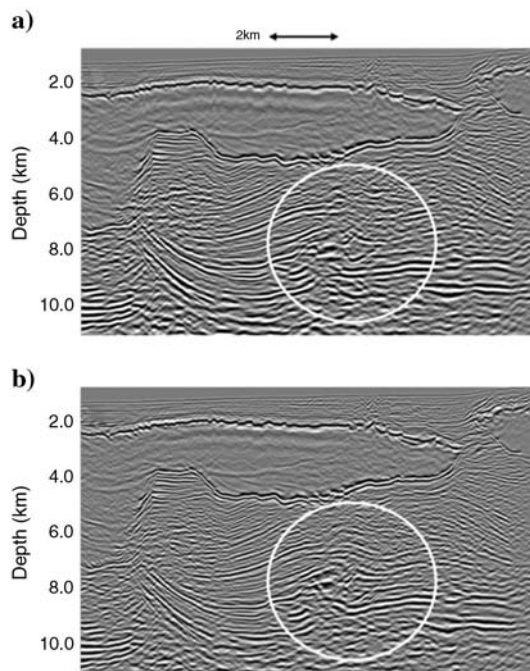


Figure 16. (a) RTM image before DIT scans; (b) RTM image after DIT scans.

### RTM-based delayed imaging time scans

Although the velocity perturbation scan technique is promising, the cost of generating a seismic migration scan is still comparatively high, and it requires multiple prestack migration runs. To address the cost issues, Wang et al. (2006, 2009) have developed a new efficient subsalt velocity updating approach using RTM-based delayed imaging time (DIT) scans. In DIT scan, only one RTM run is performed, but multiple migration scan images are formed by applying zero time as well as nonzero time (such as  $-200$  ms or  $+200$  ms) (Sava and Fomel, 2006; Wang et al., 2006) imaging conditions, as explained earlier. Since application of additional imaging conditions can be performed at a very small fraction of the cost as compared with the whole RTM run, typically dense scans (such as 21 scans) are produced.

Figure 15 shows an example of DIT-scan panels. Clearly, for this example, with the negative time-shift, the subsalt events are much better focused. Figure 16 shows a 3D example from Gulf of Mexico, comparing the RTM images before and after the DIT subsalt velocity update. In the highlighted target area, after the DIT scans, the RTM image is much more interpretable, and our interpreters believe the new structure makes more geological sense.

### CONCLUSIONS

In this paper we have presented the fundamental ideas underlying subsalt imaging. The physical problem caused by the presence of thick allochthonous salt sheets surrounded by acoustic softer sediments is an illumination issue related to the geometry of the sediment-salt interface. We have summarized the four types of prestack depth imaging algorithms that are currently the industry's preferred imaging methods and described their strengths and weaknesses. In addition the rich spectrum of imaging conditions was investigated. Finally, we have described the elements of the model building and

some techniques for subsalt velocity updates. While a huge amount of progress has been made in this field, yielding great improvement in image quality, we fully expect that the subsalt challenge will continue to spur new theoretical developments and processing techniques, in the quest for yet more accurate and precise subsurface images.

## REFERENCES

- Albertin, U., S. J. Kapoor, and W. Chang, 1998a, Velocity resolution and salt boundary placement in subsalt imaging: Part 1: 68th Annual International Meeting, SEG, Expanded Abstracts, 1297–1300.
- Albertin, U., S. J. Kapoor, W. Chang, R. Beals, and J. Curtis, 1998b, Velocity resolution and salt boundary placement in subsalt imaging: Part 2: 68th Annual International Meeting, SEG, Expanded Abstracts, 1301–1304.
- Albertin, U., M. Woodward, J. Kapoor, W. Chang, S. Charles, D. Nichols, P. Kitchenside, and W. Mao, 2001, Depth imaging examples and methodology in the Gulf of Mexico: *The Leading Edge*, **20**, 498–513, doi: [10.1190/1.1438980](https://doi.org/10.1190/1.1438980).
- Anderson, J. E., and C. M. Marcinkovich, 2005, Finding the edge of salt via a dual-velocity flood: 75th Annual International Meeting, SEG, Expanded Abstracts, 1974–1977.
- Audebert, F., and J. P. Diet, 1996, CRP-scan from 3D prestack depth migration: A new tool for velocity model building: 58th Annual International Conference, EAGE, Extended Abstracts, X011.
- Baysal, E., D. Kosloff, and J. W. C. Sherwood, 1983, Reverse-time migration: *Geophysics*, **48**, 1514–1524, doi: [10.1190/1.1441434](https://doi.org/10.1190/1.1441434).
- Beylkin, G., 1985, Imaging of discontinuities in the inverse scattering problem by inversion of a causal generalized radon transform: *Journal of Mathematical Physics*, **26**, 99–108, doi: [10.1063/1.526755](https://doi.org/10.1063/1.526755).
- Billette, F. J., and S. Brandsberg-Dahl, 2005, The 2004 BP velocity benchmark: 67th EAGE Meeting, B035.
- Biondi, B., 2011, Velocity estimation by image focusing analysis: *Geophysics*, **75**, no. 6, U49–U60.
- Bleistein, N., 1987, On the imaging of reflectors in the earth: *Geophysics*, **52**, 931–942, doi: [10.1190/1.1442363](https://doi.org/10.1190/1.1442363).
- Cerveny, V., M. M. Popov, and I. Psencik, 1982, Computation of wave fields in inhomogeneous media Gaussian beam approach: *Geophysical Journal of the Royal Astronomical Society*, **70**, 109–128.
- Claerbout, J. F., 1971, Toward a unified theory of reflector mapping: *Geophysics*, **36**, 467–481, doi: [10.1190/1.1440185](https://doi.org/10.1190/1.1440185).
- Claerbout, J. F., 1985, *Imaging the earth's interior*: Blackwell Scientific Publications.
- Cohen, J. K., F. G. Hagin, and N. Bleistein, 1986, Three dimensional born inversion with an arbitrary reference: *Geophysics*, **51**, 1552–1558, doi: [10.1190/1.1442205](https://doi.org/10.1190/1.1442205).
- Corcoran, C., C. Perkins, D. Lee, P. Cattermole, R. Cook, and R. Moldoveanu, 2007, A wide-azimuth streamer acquisition pilot project in the Gulf of Mexico: *The Leading Edge*, **26**, 460–468, doi: [10.1190/1.2723210](https://doi.org/10.1190/1.2723210).
- Costa, C. A., S. Raz, and D. Kosloff, 1989, Gaussian beam migration: 59th Annual International Meeting, SEG, Expanded Abstracts, 1169–1171.
- de Bruin, C., C. Wapenaar, and A. J. Berkhout, 1990, Angle-dependent reflectivity by means of prestack migration: *Geophysics*, **55**, 1223–1234, doi: [10.1190/1.1442938](https://doi.org/10.1190/1.1442938).
- Fomel, S., 2004, Theory of 3-d angle gathers in wave-equation imaging: 74th Annual International Meeting, SEG, Expanded Abstracts, 1053–1056.
- French, W. S., 1974, Two-dimensional and three-dimensional migration of model-experiment reflection: *Geophysics*, **39**, 265–277, doi: [10.1190/1.1440426](https://doi.org/10.1190/1.1440426).
- Hale, D., N. R. Hill, and J. P. Stefani, 1992, Imaging salt with turning seismic waves: *Geophysics*, **57**, 1453–1462, doi: [10.1190/1.1443213](https://doi.org/10.1190/1.1443213).
- Haugen, J. A., B. Arntsen, and J. Mispel, 2008, Modeling of dirty salt: 78th Annual International Meeting, SEG, Expanded Abstracts, 2127–2131.
- Hemon, C., 1978, Wave equations and models: *Geophysical Prospecting*, **26**, 790–821, doi: [10.1111/gpr.1978.26.issue-4](https://doi.org/10.1111/gpr.1978.26.issue-4).
- Hill, N. R., 1990, Gaussian beam migration: *Geophysics*, **55**, 1416–1428, doi: [10.1190/1.1442788](https://doi.org/10.1190/1.1442788).
- Howard, M., and N. Moldoveanu, 2006, Marine survey design for rich-azimuth seismic using surface streamers: *The Leading Edge*, **25**, 2915–2919.
- Hudec, M. R., and M. P. A. Jackson, 2007, Terra infirma: understanding salt tectonics: *Earth-Science Reviews*, **82**, 1–28, doi: [10.1016/j.earscirev.2007.01.001](https://doi.org/10.1016/j.earscirev.2007.01.001).
- Jiao, J., D. Lowrey, J. Willis, and D. Solan, 2006, An improved methodology for sub-salt velocity analysis: 76th Annual International Meeting, SEG, Expanded Abstracts, 3105–3108.
- Jones, I. F., 2008, A modeling study of pre-processing considerations for reverse-time migration: *Geophysics*, **73**, no. 6 T99–T106, doi: [10.1190/1.2981183](https://doi.org/10.1190/1.2981183).
- Jones, I. F., 2010, *An introduction to velocity model building*: European Association of Geoscientists & Engineers.
- Jones, I. F., H. Baud, K. Ibbotson, and F. Audebert, 2000, Continuous 3D preSDM velocity analysis: *The Leading Edge*, **19**, no. 3, 263–269, doi: [10.1190/1.1438584](https://doi.org/10.1190/1.1438584).
- Jones, I. F., K. Ibbotson, M. Grimshaw, and P. Plasterie, 1998, 3D pre-stack depth migration and velocity model building: *The Leading Edge*, **17**, 897–911, doi: [10.1190/1.1438063](https://doi.org/10.1190/1.1438063).
- Kapoor, J., N. Moldevaneau, M. Egan, M. O'Briain, D. Desta, L. Atakishiyev, M. Tomida, and L. Stewart, 2007, Subsalt imaging: The RAZ-WAZ experience: *The Leading Edge*, **26**, 1414–1422, doi: [10.1190/1.2805764](https://doi.org/10.1190/1.2805764).
- Kapoor, J., and M. Woodward, 2008, Velocity model building for subsalt imaging using wide and rich azimuth data: 78th Annual International Meeting, SEG, Expanded Abstracts, 3693–3696.
- Kelly, S., and R. Jiayang, 2004, Key elements in the recovery of relative amplitude for prestack shot record migration: *The Leading Edge*, **23**, 882–886, doi: [10.1190/1.1803497](https://doi.org/10.1190/1.1803497).
- Leveille, J. P., K. Larner, and J. Higginbotham, 2005, A problem workshop: *The Leading Edge*, **24**, 1126–1132, doi: [10.1190/1.2135107](https://doi.org/10.1190/1.2135107).
- Lewis, J., 2006, The potential of mode-converted waves in salt interpretation: Presented at SEG/EAGE summer research workshop.
- Liu, F., G. Zhang, S. A. Morton, and J. P. Leveille, 2011, An effective imaging condition for reverse-time migration using wavefield decomposition: *Geophysics*, **76**, no. 1, S29–S39, doi: [10.1190/1.3533914](https://doi.org/10.1190/1.3533914).
- McMechan, G. A., 1983, Migration by extrapolation of time-dependent boundary values: *Geophysical Prospecting*, **31**, 413–420, doi: [10.1111/gpr.1983.31.issue-3](https://doi.org/10.1111/gpr.1983.31.issue-3).
- Moldoveanu, N., J. Kapoor, and M. Egan, 2008, Full-azimuth imaging using circular geometry acquisition: *The Leading Edge*, **27**, 908–913, doi: [10.1190/1.2954032](https://doi.org/10.1190/1.2954032).
- Nolan, C., and W. Symes, 1996, *Imaging in complex velocities with general acquisition geometry*: Trip, The Rice Inversion Project, Rice University.
- Pratt, R. G., 2003, *Waveform tomography: Theory and practice*. An invited presentation given at the 12th international workshop on controlled-source seismology: Mountain Lake, Virginia (web link @ <http://geol.queensu.ca/people/pratt/prattccss.pdf>).
- Rickett, J. E., and P. C. Sava, 2002, Offset and angle-domain common image-point gathers for shot-profile migration: *Geophysics*, **67**, 883–889, doi: [10.1190/1.1484531](https://doi.org/10.1190/1.1484531).
- Ritter, G., 2010, Interpretation driven velocity model building to improve subsalt imaging: 81st Annual International Meeting, SEG, Expanded Abstracts, 4098–4102.
- Sava, P., and S. Fomel, 2003, Angle-domain common-image gathers by wave field continuation methods: *Geophysics*, **68**, 1065–1074, doi: [10.1190/1.1581078](https://doi.org/10.1190/1.1581078).
- Sava, P., and S. Fomel, 2006, Time-shift imaging condition in seismic migration: *Geophysics*, **71**, no. 6, S209–S217, doi: [10.1190/1.2338824](https://doi.org/10.1190/1.2338824).
- Sava, P., and I. Vasconcelos, 2011, Extended imaging conditions for wave-equation migration: *Geophysical Prospecting*, **59**, 35–55, doi: [10.1111/gpr.2010.59.issue-1](https://doi.org/10.1111/gpr.2010.59.issue-1).
- Schneider, W. A., 1978, Integral formulation for migration in two and three dimensions: *Geophysics*, **43**, 49–76, doi: [10.1190/1.1440828](https://doi.org/10.1190/1.1440828).
- Sexton, P., B. Duquet, J. L. Bourouillec, F. Adler, V. Martin, and M. Stankoff, 2009, Block 32, Angola—a case study in complex imaging: EAGE, Subsalt Imaging Workshop, SS29.
- Sherwood, J. W. C., K. Sherwood, H. Tieman, and K. Schleicher, 2008, 3d beam prestack depth migration with examples from around the world: 78th Annual International Meeting, SEG, Expanded Abstracts, 438–442.
- Wang, B., V. Dirks, P. Guillaume, F. Audebert, and D. Epili, 2006, A 3D subsalt tomography based on wave-equation migration-perturbation scans: *Geophysics*, **71**, no. 2, E1–E6, doi: [10.1190/1.2187720](https://doi.org/10.1190/1.2187720).
- Wang, B., V. Dirks, P. Guillaume, F. Audebert, A. Hou, and D. Epili, 2004, 3D sub-salt tomography based on wave equation migration perturbation scans: 74th Annual International Meeting, SEG, Expanded Abstracts, 2375–2378.
- Wang, B., Y. Kim, C. Mason, and X. Zeng, 2008, Advances in velocity model-building technology for subsalt imaging: *Geophysics*, **73**, no. 5, VE173–VE181, doi: [10.1190/1.2966096](https://doi.org/10.1190/1.2966096).
- Wang, B., C. Mason, M. Guo, K. Yoon, J. Cai, J. Ji, and Z. Li, 2009, Subsalt velocity update and composite imaging using reverse-time-migration based delayed-imaging-time scan: *Geophysics*, **74**, no. 6, WCA159–WCA167, doi: [10.1190/1.3227152](https://doi.org/10.1190/1.3227152).
- Wang, B., D. Wheaton, F. Audebert, and V. Dirks, 2006, Separation of focusing and positioning effects using wave equation based focusing analysis and post-stack modeling: 76th Annual International Meeting, SEG, Expanded Abstracts, 2646–2649.

- Whitmore, D., 1983, Iterative depth migration by backward time propagation: 53rd Annual International Meeting, SEG, Expanded Abstracts, 382–385.
- Woodward, M., D. Nichols, O. Zdraveva, P. Whitfield, and T. Johns, 2008, A decade of tomography: *Geophysics*, **73**, no. 5, VE5–VE11, doi: [10.1190/1.2969907](https://doi.org/10.1190/1.2969907).
- Xu, S., H. Chauris, G. Lambare, and M. Noble, 2001, Common-angle migration: A strategy for imaging complex media: *Geophysics*, **66**, 1877–1894, doi: [10.1190/1.1487131](https://doi.org/10.1190/1.1487131).
- Xu, S., Y. Zhang, and B. Tang, 2010, 3D common image gathers from reverse time migration: 81st Annual International Meeting, SEG, Expanded Abstracts, 3257–3262.
- Zhang, Q., and G. A. McMechan, 2011, A DCIG for isotropic RTM direct vectorfield method to obtain angle-domain common-image gathers from isotropic acoustic and elastic reverse-time migration: *Geophysics*, submitted.
- Zhang, Y., and J. Sun, 2009, Practical issues of reverse-time migration: True amplitude gathers, noise removal and harmonic-source encoding: *First Break*, **26**, 19–25.
- Zhang, Y., S. Xu, N. Bleistein, and G. Zhang, 2007, True-amplitude, angle-domain, common-image gathers from one-way wave-equation migrations: *Geophysics*, **72**, no. 1, S49–S58, doi: [10.1190/1.2399371](https://doi.org/10.1190/1.2399371).
- Zhang, Y., G. Zhang, and N. Bleistein, 2002, Theory of true amplitude common-shot migration: 72nd Annual International Meeting, SEG, Expanded Abstracts, 2471–2474.
- Zhang, Y., G. Zhang, and N. Bleistein, 2005, Theory of true amplitude one-way wave equations and true amplitude common-shot migration: *Geophysics*, **70**, no. 4, E1–E10, doi: [10.1190/1.1988182](https://doi.org/10.1190/1.1988182).